PAPER

Check for updates

Enhanced stability and complex phase behaviour of organic–inorganic green-emitting ionic manganese halides†

Brando Adranno,[a] Veronica Paterlini,[a] Volodymyr Smetana, [ID] [a,b] Guillaume Bousrez, [ID] [a,b] Alexander Ovchinnikov [ID] [a] and Anja-Verena Mudring [ID] ⋆[a,b]

Light-emitting materials based on earth-abundant metals, such as manganese hold great promise as emitters for organic lighting devices. In order to apply such emitter materials and, in particular, to overcome the problem of self-quenching due to cross-relaxation, we investigated a series of tetrabromido-manganate ($[MnBr_4]^{2-}$) salts with bulky tetraalkylphosphonium counter cations $[P_{nnn}]^+$, namely $[P_{nnnn}]_2[MnBr_4]$ (n = 4 (**1**), 6 (**2**) and 8 (**3**)), which can be obtained by a straightforward reaction of the respective phosphonium bromide and $MnBr_2$. Variation of the cation size allows control of the properties of the resulting ionic materials. **1** and **3** qualify as ionic liquids (ILs), where **1** features a melting point of 68 °C, and **3** is liquid at room temperature and even at very low temperatures. Furthermore, **1** and **2** show the formation of higher-ordered thermotropic mesophases. For **1** a transition to a thermodynamically metastable smectic liquid crystalline phase can be observed at room temperature upon reheating from the metastable glassy state; **2** appears to form a plastic crystalline phase at ~63 °C, which persists up to the melting point of 235 °C. The photoemission is greatly affected by phase behaviour and ion dynamics. A photoluminescence quantum yield of 61% could be achieved, by balancing the increase in Mn^{2+}-Mn^{2+} separation and reducing self-quenching through increasingly large organic cations which leads to adverse increased vibrational quenching. Compared to analogous ammonium compounds, which have been promoted as ˝inorganic hybrid perovskites˝, the phosphonium salts show superior performance, with respect to photoluminescent quantum yield and thermal and air/humidity stability. As the presented compounds are not sensitive to the atmosphere, in particular moisture, and show strong visible electroluminescence in the green region of light, they are important emitter materials for use in organic light-emitting devices.

[a]*Department of Materials and Environmental Chemistry, Stockholm University, Svante Arrhenius väg 16C, SE-10691 Stockholm, Sweden. E-mail: anja-verena.mudring@mmk.su.se, anja-verena.mudring@bce.au.dk*
[b]*Intelligent Advanced Materials, Department of Biological & Chemical Engineering and iNANO, Aarhus University, 8000 Aarhus C, Denmark*

Introduction

In the last decades, the field of lighting technology has seen an increasingly high number of studies aimed at the design of efficient and sustainable materials and devices. More specifically, extremely promising results have been obtained from organic lighting devices, such as organic light-emitting diodes (OLEDs) and light-emitting electrochemical cells (LECs).[2,3]

Despite differences in their working mechanisms and structure, both types of devices often utilise hybrid organic–inorganic or organic materials as light emitters. The most efficient emitting materials for organic lighting are usually based on compounds containing noble metals, particularly iridium(III), platinum(II), and ruthenium(II),[3,5–12] with high efficiency resulting from the triplet harvesting effect.[13] These materials allow emission from a triplet excited state, which is further enhanced by relativistic effects.[14] Since the electrochemically generated excitons are distributed between the singlet and triplet states in a 1 : 3 ratio, respectively, due to spin statistics, the utilisation of triplet phosphorescent emitters offers higher performance as compared to conventional devices employing fluorescent emitters.[15–18] However, the majority of these materials have demonstrated limited stability and a short lifetime, especially for the emission of blue and green light. Although some progress has been made to overcome these issues,[10,11,19] the heavy metals generally utilised have a

low natural abundance and high costs, which further limit their practical application. This has motivated us to investigate the luminescent properties of materials based on more earth-abundant metals.

In this respect, manganese(II) complexes have been one class of materials that have received vast attention due to their wide array of luminescent properties (*i.e.* triboluminescence, electroluminescence, photoluminescence, and temperature dependency) which have been extensively studied.[20–23] The luminescence of these complexes with $3d^5$ valence configuration is ruled by the d–d transition between the quartet excited state, $^4T_1$, and the sextet ground state, $^6A_1$. Due to the spin-forbidden nature of the transition, it can only be achieved as a result of spin–orbit coupling. Therefore, luminescence is considerably influenced by the symmetry of the coordination environment.[24–27] Furthermore, the energies of the electronic states are affected by the ligand field strength.[21] For these reasons, the choice of the ligands and the counterions (if present) is crucial to achieving specific emission wavelengths and luminescence efficiency. Non-centrosymmetric, tetrahedral complexes typically provide green emission (weak ligand field), while centrosymmetric, octahedral ones produce red emission (strong ligand field). Emitting Mn(II) complexes can be both neutral or ionic, depending on the nature of the ligands. The most commonly studied ions with tetrahedrally coordinated Mn(II) are $[MnX_4]^{2-}$ anions, where X is a halogen. These anions are usually charge-balanced by organic cations, acting as bulky spacers that prevent the self-quenching of neighbouring Mn(II) complexes. The correlation between the proximity of manganese centres and the photoluminescence quantum yield (PLQY) has been recently reported by Mao and collaborators,[28] who demonstrated that a long average Mn–Mn distance (>9 Å) promotes luminescence. Long distances between the Mn(II) cations reduce the chance of energy transfer in hybrid organic–inorganic materials, increasing the chance of emission. A representative example is bis(tetraphenylphosphonium) tetrabromidomanganate(II) ($[PPh_4]_2[MnBr_4]$), where the minimum Mn–Mn distance is found to be 10.45(1) Å.[29] In this compound, the anion $[MnBr_4]^{2-}$ is surrounded by an extremely rigid environment created by the phenyl rings of the phosphonium cations, which keep the Mn(II) centres apart. This compound has additionally been proved feasible for application in light-emitting devices displaying an external quantum efficiency of up to 9.6%.[29,30] Several ionic manganese-based emitters containing phosphonium cations as counterions functionalised by at least one aromatic ring are known.[29,31–41] However, to the best of our knowledge, no such light-emitting compounds have been reported based on tetraalkylphosphonium cations, except the brief results presented by Howard and Sundheim in 1969,[42] where the persistent green luminescence in the molten state of bis(tetrabutylammonium) and bis(tetrabutylphosphonium) tetrabromidomanganate was described. In the period between that study and today, the research on Mn(II) emitters based on tetraalkylammonium cations led to several materials, which have also seen application in electrochemical luminescent devices.[36,39,43–52] Nonetheless, these were always

characterised by short organic chains with up to four carbon atoms.

Taking advantage of our expertise in ionic liquids (ILs), we saw the lacunae in the tetraalkylphosphonium-based materials and the small range of explored organic chains as an opportunity to design green-emitting ionic materials with specific thermal properties. It is known that the length of the alkyl chains attached to the cationic or anionic units of an IL has a tremendous effect on the thermal behaviour of the final material. The formation of mesophases, glass transitions, and melting points are some of the easily tuneable properties of the phosphonium-based ILs.[53] Additionally, these are normally characterised by a higher thermal and chemical stability compared to the N-based ILs (*i.e.*, with imidazolium, ammonium, or pyridinium cations);[54] additionally, they have been successfully applied as electrolytes in lithium batteries and solar cells.[55] Therefore, it is of undoubted interest to investigate the potential of Mn(II) emitters integrating tetraalkylphosphonium cations. In such compounds, the alkyl chains may keep the emitting centres apart to ensure efficient emission, while the IL character of the final material could allow the use of simple solvent-free techniques for layer deposition in light-emitting devices.[56]

In this contribution, we synthesised and characterised a series of three bis(tetraalkylphosphonium) tetrabromidomanganates $[P_{nnnn}]_2[MnBr_4]$ (n = 4, 6, 8). Our purpose was to find the right balance between photophysical and thermal properties in order to tailor these materials for possible applications as emitting layers in electrochemical devices.

Experimental

Synthesis of bis(tetrabutylphosphonium) tetrabromidomanganate $[P_{4444}]_2[MnBr_4]$ (1), bis(tetrahexylphosphonium) tetrabromidomanganate $[P_{6666}]_2[MnBr_4]$ (2), and bis(tetraoctylphosphonium) tetrabromidomanganate $[P_{8888}]_2[MnBr_4]$ (3)

All reagents and solvents were purchased from Sigma Aldrich (Steinheim, Germany) and used without further purification. Phosphonium bromides were prepared following a procedure adapted from a previously reported one.[57] The respective phosphonium bromide (10 mmol, 2 eq.) was dissolved in acetonitrile (50 mL). Manganese(II) bromide (5 mmol, 1 eq.) was then added while stirring to yield a light yellow solution. After stirring overnight, the solvent was removed under reduced pressure to give a light yellow-green solid (1 and 2) or a dark yellow-orange viscous liquid (3). The materials were subsequently washed with ethyl acetate and dried under vacuum. All materials were produced in quantitative yield based on the final weight of the products.

$[P_{4444}]_2[MnBr_4]$ (1), light yellow-green solid. ESI TOF: m/z (negative mode, $[MnBr_4]^{2-}$) 188.0445 (calculated m/z = 187.3042).

FTIR: ν_{max} (cm^{-1}) = 3492, 2957, 2928, 2870, 2731, 1637, 1463, 1407, 1379, 1346, 1314, 1285, 1228, 1192, 1122, 1098, 1053, 1005, 967, 918, 812, 789, 752, 717, 504, 454, 432, 400.

[P$_{6666}$]$_2$[MnBr$_4$] (2), light yellow-green solid. ESI TOF: m/z (negative mode, [MnBr$_4$]$^{2-}$) 188.0445 (calculated m/z = 187.3042).

FTIR: $\nu_{\max}$ (cm^{-1}) = 2955, 2925, 2858, 1457, 1408, 1378, 1317, 1301, 1265, 1247, 1213, 1175, 1110, 1044, 991, 891, 859, 807, 716, 586, 543, 509, 481, 469, 456, 435, 412.

[P$_{8888}$]$_2$[MnBr$_4$] (2), dark orange-yellow oil. ESI TOF: m/z (negative mode, [MnBr$_4$]$^{2-}$) 188.0445 (calculated m/z = 187.3042).

FTIR: $\nu_{\max}$ (cm^{-1}) = 2955, 2923, 2854, 1635, 1458, 1408, 1377, 1303, 1264, 1241, 1200, 1166, 1115, 1032, 938, 851, 808, 768, 720, 515, 435, 400.

Thermogravimetric analysis (TGA) confirmed that anhydrous compounds had been obtained. The materials were kept in vials in air, and Karl Fischer titration showed only minimal water uptake over a few months (Table S1†).

Instrumentation

Infrared spectroscopy

IR spectra were collected with a Bruker Alpha-P ATR-spectrometer (Karlsruhe, Germany) in an attenuated total reflection configuration. Data processing was carried out with the program, OPUS (Bruker, Karlsruhe, Germany).

Raman spectroscopy

Room temperature Raman spectra ranging from 100 to 4000 cm^{-1} were recorded with a Horiba LabRAM HR system (Horiba, Japan) using a red LASER (λ = 785 nm), a CCD detector, and a Si standard (520.5 cm^{-1} line) for calibration.

Karl-fischer titration

Coulometric Karl Fischer titration measurements were carried out with a C10S KF Coulometer (Mettler Toledo, Sweden).

Single crystal X-ray diffraction

Attempts to grow crystals of **1** and **2** suitable for SCXRD via isothermal evaporation of acetonitrile, ethanol, and methanol solutions under ambient conditions were not successful. Therefore, different crystal growth strategies were undertaken.

Crystals of **1** were obtained by first melting the sample in air and then blast-freezing the obtained liquid at −20 °C. For SCXRD data collection, crystals were gathered on a fibre glass holder at −80 °C and then placed in the diffractometer pre-set at −173 °C.

Single-crystal X-ray diffraction data of **1** were recorded at 100 K and room temperature using a Bruker D8 Venture diffractometer (Mo Kα, λ = 0.7107 Å). Data reduction was performed with the program package, X-Red or SAINT, and absorption corrections were carried out with the programs, X-Shape or SADABS. Crystal structure determination was carried out using SHELXT[58] within Olex2.[59] Refinement was performed with SHELXL.[60] Hydrogen atoms were added according to the riding atom model. The programs,

Diamond[61] and Mercury,[62] were used to illustrate the resulting structure.

Powder X-ray diffraction

Powder X-ray diffraction (PXRD) data of **1** and the LTS of **2** were recorded at ambient temperature on a PANalytical X′pert PRO diffractometer (Malvern Panalytical, Malvern, UK), operating using Cu Kα1 radiation (λ = 1.5406 Å). The PXRD data at 50 °C were collected on a Bruker Phaser D2 diffractometer (Bruker AXS, Karlsruhe, Germany) equipped with Cu Kα radiation (λ = 1.5418 Å). The data collection was conducted in reflection mode from 5° to 70°2Θ with a rate of 0.55 sec/step. The predicted PXRD diffractogram of **1** was calculated based on the model refined from the single-crystal X-ray diffraction data using the program Mercury.[62]

Thermogravimetric analysis

Thermogravimetric analysis (TGA) was performed with a TG 449 F3 Jupiter (Netzsch, Selb, Germany) using aluminium oxide crucibles at a heating rate of 10 °C min^{-1} with argon as a purge gas. The given temperatures correspond to the 5% onset of the respective thermal process.

Differential scanning calorimetry

Differential scanning calorimetry (DSC) was performed with a computer-controlled Mettler Toledo thermal analyzer (Sweden). The experiments were carried out using a heating rate of 1 °C min^{-1} in a sealed aluminium crucible with a nitrogen flow rate of 50 mL min^{-1}. The samples were placed in small aluminium containers, which were cold-sealed and punctured. Given temperatures correspond to the peak of the respective thermal process.

Polarised optical microscopy

Optical analyses were conducted by heated-stage polarised optical microscopy (POM) with an Axio Imager A1 microscope (Carl Zeiss MicroImaging GmbH, Göttingen, Germany) equipped with a hot stage, THMS600 (Linkam Scientific Instruments Ltd, Surrey, UK), and Linkam TMS 94 temperature controller. Images were recorded at a magnification of 50× as a video with a digital camera. Heating and cooling rates were 1 °C min^{-1}.

UV-Vis absorption spectroscopy

The UV-Vis absorption spectra were recorded using an Agilent Technologies Cary 5000 UV-Vis-NIR spectrophotometer equipped with an Agilent Praying Mantis diffuse reflectance accessory (Agilent Technologies, Kista, Sweden). A Spectralon$^©$ disk was used as the reference material for the measurements on powders of **1** and **2**. The absorbance of **3** was recorded by spreading the viscous liquid on the internal surface of a cuvette, and the air was used as the reference.

Optical spectroscopy

Steady-state fluorescence excitation, emission spectra, and fluorescence decays were recorded on a HORIBA Jobin Yvon

FluoroLog-3 modular spectrofluorometer with an R928P PMT detector (Horiba France, Longjumeau, France), a double excitation monochromator and a single emission monochromator. A 450 W xenon continuous lamp was used for the steady-state measurements, whereas a pulsed Xe lamp was used for lifetime measurements. Quantum Yields (QYs) were determined with an integrating sphere using $BaSO_4$ as a reference.

Cyclic voltammetry

Cyclic voltammetry analysis was conducted on a Gamry Instrument Interface 1010 potentiostat (Warminster, Pennsylvania, United States) using a three-electrode method. Glassy carbon (d = 3 mm) was used as a working electrode, Pt coil as a counter electrode, and a capillary with septum containing an Ag rod that was submerged into a solution of 0.1 M $LiTf_2N$ in N_2-saturated acetonitrile were used as a reference electrode. Multiple scans were conducted at 100 mV s^{-1} on a 10^{-3} M solution of $[P_{4444}]_2[MnBr_4]$ (**1**), $[P_{6666}]_2[MnBr_4]$ (**2**) and $[P_{8888}]_2[MnBr_4]$ (**3**) in acetonitrile. $LiTf_2N$ was used as a supporting electrolyte.

Results and discussion

Synthetic procedure

To obtain the respective bis(tetraalkylphosphonium) tetrabromidomanganates(II) $[P_{nnnn}]_2[MnBr_4]$ with n = 4, 6, or 8, an acetonitrile solution of the corresponding tetraalkylphosphonium bromide $[P_{nnnn}Br]$ and $MnBr_2$ in a 1 : 2 molar ratio was stirred overnight under ambient conditions (Scheme 1). After removing the solvent under reduced pressure, the final products (**1**–**3**) were obtained in quantitative yields. Compounds **1** and **2** are light yellow-green waxy powders, while **3** was collected as a dark yellow-orange viscous liquid.

Vibrational spectroscopy

The first structural characterisation was undertaken by means of vibrational spectroscopy. The recorded infrared (FTIR) spectra show the signatures of the respective phosphonium cations, such as the characteristic highly intense C–H stretching modes in the range 2750–3000 cm^{-1} and the C–H bending modes in the range 1300–1450 cm^{-1} (ESI, Fig. S1–S3†). The absence of vibrations in the area between 3000 cm^{-1} and 3500 cm^{-1} confirms that the products are anhydrous (for results of Coulometric Karl-Fischer titration see Table S1, ESI†.).
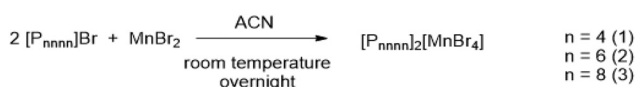
The immediate coordination of the Mn(II) was further investigated by Raman spectroscopy (ESI, Fig. S4–S6†), as the metal–ligand vibrations of tetrahedrally coordinated Mn^{2+} are both infrared- and Raman-active. For distorted $[MnBr_4]^{2-}$ tetra-

hedra, as observed in the respective tetraalkylammonium compounds,[56,57] the totally symmetric A_1 Mn–Br stretching is typically found around 157 cm^{-1} and the F_2 modes between 205–225 cm^{-1}.[63] Indeed, for **1**, the symmetric mode is observed at 158 cm^{-1}, whilst for **2** and **3**, it is found at 156 cm^{-1}. The asymmetric modes could be identified as shoulders at 216 cm^{-1} for **1** and at 210 cm^{-1} for **2** and **3**.

X-ray diffraction studies

Crystals of sufficient quality for single crystal X-ray diffraction analysis of **1** could be obtained from the melt. The compound crystallises monoclinic in the space group $P2_1/c$ with two symmetry-independent tetrabutylphosphonium cations and one $[MnBr_4]^{2-}$ moiety in the asymmetric unit (ESI, Table S2†). The Mn^{2+} ion is coordinated by four Br$^-$ in a tetrahedra-like arrangement forming isolated $[MnBr_4]^{2-}$ anions. The tetrahedron is slightly distorted with $d_{Mn–Br}$ = 2.495–2.520(1) Å and $\angle$Br–Mn–Br = 105.8–113.5(1)°. In **1**, the Mn–Br interatomic distances are slightly larger, and the angle distribution is broader in comparison to the analogous ammonium compound $[N_{4444}]_2[MnBr_4]$. The latter compound is dimorphic, while polymorphism has not been observed for **1**.[39,50] None of the two polymorphs of $[N_{4444}]_2[MnBr_4]$ crystallise isotypic with $[P_{4444}]_2[MnBr_4]$. In contrast to what is observed for the tetrahedra-like tetrabutylammonium cation in $[N_{4444}]_2[MnBr_4]$,[39,50] the two symmetry-independent tetrabutylphosphonium cations show a nearly planar arrangement of three butyl chains with the remaining one being essentially orthogonal to the C4C4'C4'' plane (ESI, Fig. S7†). The C4*PC4* angles within the plane are distributed over a broad range, *i.e.* 84.3(1)°, 104.9 (1)°, and 162.2(1)°. It is also worth noting that all in-plane chains are nearly linear, while the out-of-plane chain forms a hook (ESI, Fig. S7†). Both symmetry-independent cations are practically mirrored reflections of each other with only the C''' chain showing a deviation due to rotation (see ESI, Fig. S8, and Table S3†).

The crystal packing of $[P_{4444}]_2[MnBr_4]$ can be best described in terms of a layered structure. In the layers parallel to the *ab* plane the cations and the anions form checkered motifs along the *ab* diagonals, while clear separation of the cationic and the anionic layers could be observed along the *a* axis (Fig. 1). It is also worth noting that such crystal packing motifs are rather common in similar compounds and were observed also for the ammonium analogue, $[N_{4444}]_2[MnBr_4]_2$.[39,50] Each anion is surrounded by six phosphonium cations ($[P_{4444}]^+$) in the form of a distorted octahedron (Fig. S9†). The two symmetry-independent cations exhibit a different surrounding by $[MnBr_4]^{2-}$. While one cation forms four short contacts in the shape of a distorted tetrahedral arrangement, the other one establishes just three (Fig. S10†). Besides the coulombic interactions, weak hydrogen bonds enforce the packing. Eleven Br···HC contacts can be observed between the anion and the cations at distances shorter than the sum of the corresponding van der Waals radii. Predominantly, these close contacts involve the α-methylene hydrogen atoms. Each cation forms such short contacts with three anions. These interactions are however

Scheme 1 Synthetic procedure for compounds **1**–**3**.

$$2\ [P_{nnnn}]Br + MnBr_2 \xrightarrow[\text{room temperature}]{ACN} [P_{nnnn}]_2[MnBr_4] \qquad \begin{array}{l} n = 4\ (1) \\ n = 6\ (2) \\ n = 8\ (3) \end{array}$$
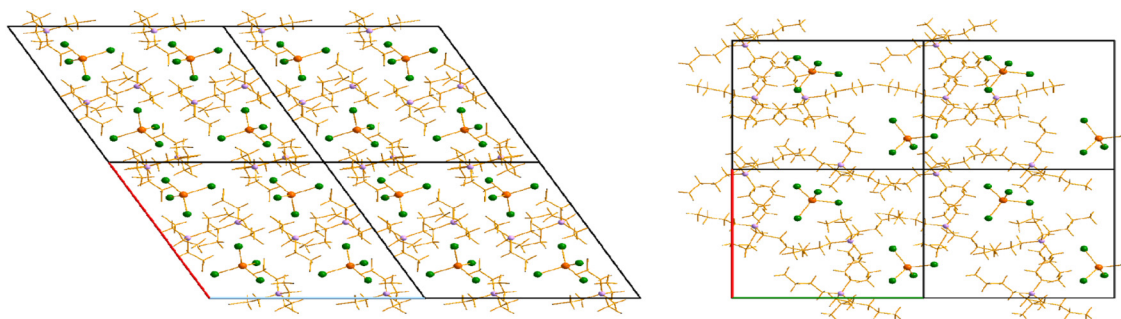
Fig. 1 Projection of the crystal structure of $[P_{4444}]_2[MnBr_4]$ (**1**) in the crystallographic *bc* plane showing the organic–inorganic layers (left) and separation of the $[MnBr_4]^{2-}$ complexes by the organic counter cations in the crystallographic *ab* plane (right). P atoms are depicted in purple, Mn atoms in orange, and Br atoms in green. The C and H atoms are omitted for clarity, but the bonds were kept to show the cation skeletons.

longer than what is normally regarded as weak hydrogen bonds,[64] and can be characterised in terms of weak electrostatic or dispersive interactions. Such weak interactions allow a high degree of rotational freedom of the alkyl chains and the anions suggesting low energy barriers required to break the crystal lattice and result in low temperatures of melting. The alkyl chains of the phosphonium cation have a strong impact on the ion packing generating intricate layered motifs. The organic layers propagate in the crystallographic *bc* plane and alternate along the *a* axis forming two phase-shifted waves with a periodicity of 16.285(2) Å (Fig. S11†). Some alkyl chains deviate from the waves forming branches (Fig. S11†) and segregating tunnels along the crystallographic *c* axis, therefore ensuring structurally isolated cavities for the $[MnBr_4]^{2-}$ anions. The $[MnBr_4]^{2-}$ tetrahedra are well separated from one another by the organic countercations (Fig. 1). The structure of $[P_{4444}]_2[MnBr_4]$ (**1**) features shortest Mn–Mn distances of 9.158 (1) Å, 9.339(1) Å, and 10.2615(18) Å. These distances are all longer than the threshold of 9 Å postulated for avoiding luminescence self-quenching;[28] they are also longer than those observed in the $P2_12_12_1$-polymorph of $[N_{4444}]_2[MnBr_4]$,[39] which features the shortest Mn–Mn distance of 8.95 Å, but shorter than those for the polymorph crystallizing in *Pnna* where an Mn–Mn distance of 10.43 Å is reported.[50]

For compound **2**, crystals could be grown *via* slow diffusion of diethyl ether as the anti-solvent in acetonitrile solution of **2** (Fig. S12†). However, the analysis of these crystals on the single-crystal X-ray diffractometer (SCXRD) revealed that all of them are of too low quality for structure determination. For compound **3**, which was obtained as a room-temperature liquid, all attempts to grow crystalline material failed .

Thermal characterisation

Thermogravimetric analyses (TGA) of **1**–**3** reveal a double-step decomposition for all compounds (Table 1 and Fig. S13–S15†). The first step occurs at 391 °C (**1**) and 383 °C (**2** and **3**), corresponding to a 75%, 80%, and 84% loss of mass, respectively, which corresponds fairly well to the loss of two $[P_{nnnn}]$Br (*n* = 4, 6 or 8) units for which the calculated values are 76%, 81%, and 84%, respectively. The second process is accompanied by an additional 14%, 12%, and 11% mass loss at 503 °C (**1**), 490 °C (**2**), and 492 °C (**3**). Compound **1** with the shorter alkyl chain phosphonium cation showed slightly higher thermal stability when compared to **2** and **3**. The thermal stability of **1** exceeds by more than 100 °C as compared to the corresponding ammonium compound, for which decomposition sets in at 220 °C.[39] The thermal phase behaviour was further investigated by a combination of differential scanning calorimetry (DSC) and hot-stage polarizing optical microscopy (POM). DSC traces for each compound are depicted in Fig. S16–S18,† while the detailed data are collected in Table 2. During the first heating cycle, **1** melts at 68.4 °C. For compari-

Table 2 The thermally induced phase transitions observed for compounds **1**, **2** and **3** after precooling the samples to −60 °C. The phase transitions are reported together with the respective onset temperatures and enthalpies

Compound	Phase transitions
1	**First cycle**

Glass ⟶ $Cr^{a)}$ — 68.4 °C (23 J/g) → $L_{iso}^{b)}$ ⟵ −34 °C

Subsequent cycles

Glass — −35 °C → L_{iso} — 22.0 °C (−17 J/g) → $SmA^{c)}$ — 61.2 °C (17 J/g) → L_{iso} ⟵ −34 °C

2	$LTS^{d)}$ — 43.1 °C (6 J/g) → $HTS^{e)}$ — 234.5 °C (10 J/g) → L_{iso} ⟵ 30.2 °C (−5 J/g) ⟵ 196.2 °C (−10 J/g)
3	No transition observed

[a] Crystalline state. [b] Isotropic liquid state. [c] Mesophase, presumably SmA. [d] Low-temperature solid phase. [e] High-temperature solid phase.

Table 1 Decomposition onset temperatures at 5% mass loss of phosphonium ILs determined with TGA

Compound	$T_{5\% \text{ onset}}$ (mass loss) (1st step) [°C]	$T_{5\% \text{ onset}}$ (mass loss) (2nd step) [°C]
$[P_{4444}]_2[MnBr_4]$ (**1**)	391 (75%)	503 (14%)
$[P_{6666}]_2[MnBr_4]$ (**2**)	383 (80%)	490 (12%)
$[P_{8888}]_2[MnBr_4]$ (**3**)	383 (84%)	492 (11%)

son, a melting point of 100 °C was reported for the analogous ammonium compound.[39] Upon cooling, **1** undergoes a glass transition at around −34 °C. In the second heating cycle, the devitrification process is observed at around −35 °C. Then, the liquid transforms in an exothermic event starting at 22.0 °C to a mesophase, which exhibits fan-conical texture when observed under polarised light pointing to a smectic A (SmA) phase (Fig. 2a). When looking at the crystal structure (Fig. 1, left) the formation of a layered mesophase seems to be pre-determined as already the solid form shows a layered structure. It could be envisioned that in the smectic phase, the layered organisation is retained, but with substantial disorder particularly in the cationic part. At higher temperatures, the DSC trace shows a second endothermic process, which is the complete melting of the compound at 61.2 °C. In the second cooling cycle, **1** transitions to the glass state at −34 °C, as it has been observed during the first cooling cycle. The third and subsequent DSC heating/cooling cycles are consistent with the second one. The crystalline phase could not be retrieved. Although the melting points of the crystalline solid and meso-phase are close in temperature, with transition temperatures of 68.4 °C and 61.2 °C, the respective heat contents show clear differences (23 J g^{-1} vs. 17 J g^{-1}), with the transition associated with the mesophase having the lower one, as expected due to the reduced order. Unfortunately, we did not succeed in obtaining X-ray diffraction data on the mesophase that would allow an unambiguous phase characterization.
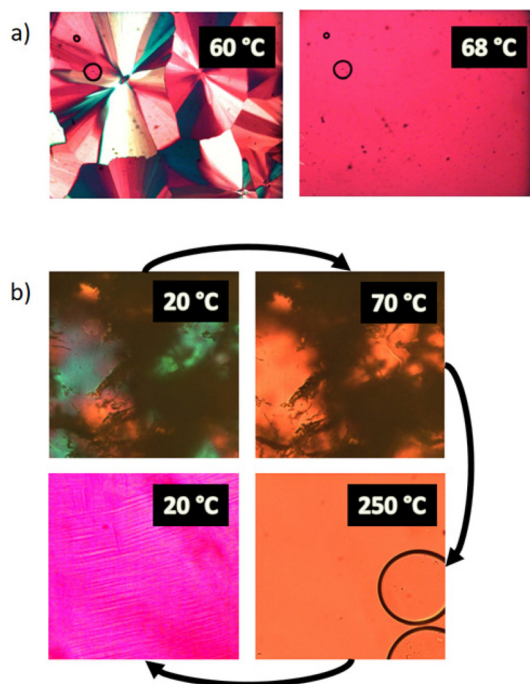
Compound **2** is solid at room temperature, and two endothermic transitions are observed during the first heating cycle: the first at 43.1 °C and the second at 234.5 °C. When inspected under the microscope, the first transition does not involve a visible change in the material's morphology, but rather a change in the ability of the material to rotate polarised light in POM as depicted in Fig. 2b. Thus, this transition is associated with conversion from a low-temperature solid phase (LTS) to a high-temperature solid phase (HTS). The second transition, at 234.5 °C, corresponds to the melting process as confirmed by POM. Upon cooling, the recrystallisation of the HTS phase was identified as an extremely sharp exothermic peak at 196.2 °C, while the conversion to the LTS phase occurs at 30.2 °C. Interestingly, while the recovery of the HTS phase was not noticeable in POM due to the absence of refraction of polarised light, a noticeable contrast in POM, which was revealed by the appearance of thin parallel lines, was observed when the LTS phase was retrieved. Subsequent DSC cycles con-sistently showed the same thermal effects.

Finally, compound **3** which was obtained as a highly viscous oil, did not show any phase transitions between −60.0 °C and 150.0 °C.

Attempts to grow single crystals for compound **2** via slow diffusion of diethyl ether as the anti-solvent in acetonitrile solution of **2** (ESI, Fig. S12†) yielded only specimens that were extremely poorly scattering, producing diffraction spots only up to a maximum resolution of only 1.89 Å. Although the col-lected data did not allow for structure determination, it was possible to index the few diffraction spots collected at room temperature with a face-centred cubic unit cell with a = 23.63 (2) Å. Upon cooling the specimens of **2** to a temperature below the phase transition temperature to −173 °C, additional reflec-tions within the same resolution limits emerged. However, unambiguous indexing of the diffraction spots was not poss-ible. Thus, we employed powder X-ray diffraction (PXRD) for crystallographic investigations of the polymorphism in **2**.
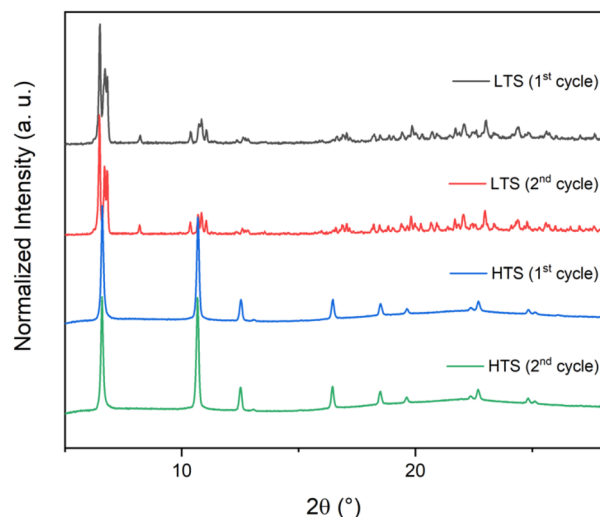

Fig. 2 (a) POM images of **1** showing conical features characteristic of an SmA phase (left) and featureless liquid phase (right). (b) POM images of **2** revealing the change of light scattering between the LTS and the HTS (top), the featureless liquid (bottom right) and the thin lines corres-ponding to the LTS (bottom left). Insets show the temperatures of observation.

Fig. 3 PXRD pattern of the LTS and HTS phases of **2** within two con-secutive heating and cooling cycles.

Temperature-dependent PXRD studies, presented in Fig. 3, confirm the transformation between the LTS and HTS. Bragg reflections of the high-temperature form (at around 50 °C) could be indexed with a face-centred cubic unit cell with a = 23.623(3) Å, which is in good agreement with the one obtained from SCXRD data. The powder patterns of the low-temperature modification (collected at 20 °C) exhibited a larger number of peaks, where the splitting of peaks can be observed along with the occurrence of additional peaks suggesting a lower crystal symmetry. Indexing of the peaks yielded a monoclinic unit cell with a = 28.130(1) Å, b = 17.224(6) Å, c = 28.627(1) Å, and β = 110.561(2)°. Analysis of the systematic extinctions indicated a C-centred cell. The unit cell volumes of the high-temperature and low-temperature modifications are 13182.7 Å^3 and 12817.7 Å^3, respectively. It is possible to transform the cubic unit cell to the monoclinic one by applying a transformation matrix (−1 1/2 1/2, 0, −1/2 1/2, 1 1/2 1/2), which provides evidence that the two modifications are structurally related. Any attempts to solve the structures from powder data were not successful. Taking the small heat content of the phase transitions into account, the observed phase relationships for **2** may indicate that the HTS corresponds to a higher-order mesophase, most likely a plastic crystalline one. Plastic crystals are materials that show one or multiple solid–solid phase transitions, corresponding to the realisation of different degrees of rotational or vibrational disorder of their molecular or ionic components.[65,66] The apparent cubic symmetry of the HTS form can then be understood as resulting from a considerable dynamic disorder of the constituting ions with preservation of their average relative positions with respect to each other, which is similar to observations made before for certain tetraalkylammonium and phosphonium compounds.[67] Upon cooling, partial quenching of the dynamic disorder and order of certain structure parts leads to a lowering of the average crystal symmetry. The thermodynamic evaluation revealed a value of residual entropy of fusion, ΔS_f = 22 J K^{-1} mol^{-1}, which falls in the characteristic range for ionic plastic crystals. As observed by MacFarlane and collaborators, ΔS_f of ionic plastic crystals normally exceeds the limit imposed by Timmerman's criterion of 20 J K^{-1} mol^{-1} for neutral molecules and it can reach up to 60 J K^{-1} mol^{-1}.[67]

As **1** revealed a melting point below 100 °C, and **3** is liquid at room temperature, they both fall in the category of ionic liquids (ILs).[68–71] It is expected that both the size and the high conformational flexibility of the tetraalkylammonium cations lower and suppress the melting point. The high degree of conformational flexibility in [P$_{8888}$]$_2$[MnBr$_4$] (**3**) is likely the reason why no transitions to a solid form could be observed upon cooling as it is kinetically hindered. For [P$_{4444}$]$_2$[MnBr$_4$] (**1**), DSC analysis shows clearly that homogeneous crystallisation is kinetically hindered. The observance of mesophase points to a delicate interplay of coulombic and secondary interionic bonding interactions. In this respect, the thermal behaviour of compound **2** is particularly interesting as, despite having alkyl chains of intermediate length within the herein presented series, **2** does not convert to an isotropic liquid below 100 °C. Generally one would expect an increase in melting point with increasing molecular weight, however, this is counteracted by reduced coulombic interaction due to the increased cation size.

Nevertheless, the enthalpy of melting observed is relatively small for a solid ionic compound, being in the range characteristic of ILs.[72] This results from the ability of two different chemical units (instead of only one) to retain a higher degree of order in the solid state prior to melting. For plastic crystals in their disordered solid state, the molecules or ions can be roughly approximated by weakly interacting spheres, with their centres of gravity occupying regular positions in the crystal lattice.[73] This is due to the rotational motion activated by flexible functional groups, e.g., alkyl chains. We believe the alkyl chains in **2** are of the right size to make the dynamically disordered phosphonium cations resemble spheres, while they appear to be too short or too long for **1** and **3**, respectively.

Photophysical properties

As we propose these kind of compounds as emitter materials for organic lightning, we investigated their photophysical properties in more detail. The excitation spectra reveal the expected transitions from the Mn^{2+} ground state ^{6}A$_1$ as a comparison with the Tanabe–Sugano diagram for d^5 the configuration shows (Fig. 4). From high to low energy, it is possible to identify seven transitions, sorted into three groups, namely F, D, and G terms. They respectively correspond to excitation to the states ^{4}T$_2$(F), ^{4}A$_2$(F) (280–300 nm), ^{4}E(D), ^{4}T$_2$(D) (350–400 nm), ^{4}A$_1$^{4}E(G), ^{4}T$_2$(G), and ^{4}T$_1$(G) (420–500 nm). Normalizing the transition energies with respect to the one with the lowest energy from absorption spectra (Fig. S20†), yields a Δ value of about 3100 cm^{-1}. The differences in alkyl chain length on the cation do not seem to affect the transition energies, but rather the relative intensities. While for **1** and **2**, the intensity of the excitation bands increases as F < D < B, in compound **3** the trend is the opposite, and the B band exhibits a more intense and broader profile. We ascribe this to **3**, in contrast to **1** and **2**, being liquid at the measurement temperature. Upon photoexcitation, all compounds show green light emission originating from the ^{4}T$_1$(G) → ^{6}A$_1$ transition of Mn^{2+}.
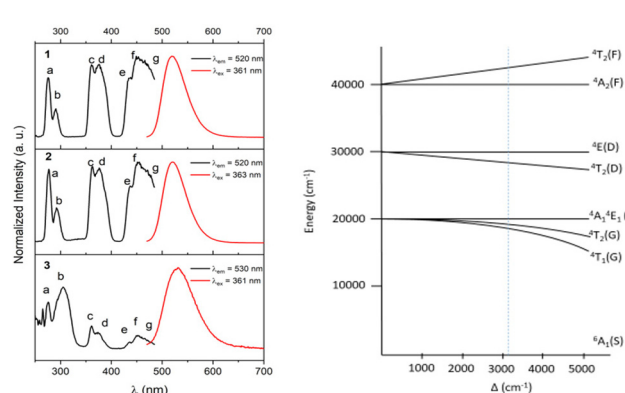

Fig. 4 (Left) Emission spectra (*red line*) and excitation spectra (*black line*) of compounds **1**–**3** collected at room temperature with the identified transitions: (a) ^{6}A$_1$ → ^{4}T$_2$(F); (b) ^{6}A$_1$ → ^{4}A$_2$(F); (c) ^{6}A$_1$ → ^{4}E(D); (d) ^{6}A$_1$ → ^{4}T$_2$(D); (e) ^{6}A$_1$ → ^{4}A$_1$^{4}E(G); (f) ^{6}A$_1$ → ^{4}T$_2$(G); (g) ^{6}A$_1$ → ^{4}T$_1$(G). (Right) Tanabe–Sugano diagram for d^5 configuration adapted from works by C. Furlani et al.[1] and Y. Rodríguez-Lazcano et al.[4]

Table 3 Lifetime and quantum yield (φ) of compounds **1–3**

Compound	λ_{em} (nm)	λ_{ex} (nm)	Lifetime (μs)	φ (%)
1	520	276	149.1 ± 0.3	55
		361	149.7 ± 0.1	61
2 (LTS)	520	276	152.4 ± 0.2	53
		363	151.9 ± 0.2	31
2 (HTS)	520	276	33.6 ± 0.1	Nd
		363	34.1 ± 0.1	Nd
3 [a]	530	276	Nd	Nd
		361	Nd	Nd

[a] Emission intensity was not sufficient to perform the analysis. (nd) not possible to determine.

Compounds **1** and **2** show maximum emission at 520 nm, while the peak for compound **3** is slightly redshifted at 530 nm (Fig. 4 and Table 3). The shift in emission wavelength of **3** may be attributed to a longer average Mn–Br interatomic distance.[74] Together with the fact that the emission band of **3** features a relatively large full width at half maximum (FWHM) of around 78 nm (2700 cm^{-1}), this points to larger structural flexibility, including the dynamic variation of the Mn–Br distance which most likely can be attributed to **3** being liquid at the measurement temperature. In comparison, the FWHM of the emissions recorded for **1** and **2** are similar, 53 nm (1925 cm^{-1}) and 54 nm (1965 cm^{-1}), respectively, in accordance with the previously reported values for solid tetrahalidomanganate compounds with organic countercations.[24] To illustrate how the human eye would perceive the emitted light the corresponding coordinates of the Commission Internationale de L'Eclairage (CIE) 1931 colour space are visualised in Fig. 5.[75]

Only compounds **1** and **2**, which are solid at room temperature, generate an intense enough emission to allow lifetime and quantum yield (φ) determination. For liquid compound **3**, vibrational quenching is too strong. The values determined exciting at 276 nm are $\varphi = 61\%$ for **1** and $\varphi = 53\%$ for **2**, and are comparable to those reported for MnBr$_4^{2-}$ complexes combined with tetraalkylammonium cations, such as [N$_{2222}$]$_2$[MnBr$_4$] (56%) and [N$_{3333}$]$_2$[MnBr$_4$] (56%).[76] The photoluminescence decays of compounds **1** and **2** can be fitted with a mono-exponential function (ESI, Fig. S21–S24†), which yields lifetimes of 149.7 μs for **1** and 152.4 μs for **2**. These values are comparable with those reported for tetraalkylammonium com-

pounds[76] and other tetrahedrally coordinated manganese halides with N-based counterions such as pyridinium and pyrrolidinium derivatives.[31,76,77]

The importance of structural rigidity and intermolecular/interionic interactions also becomes visible when comparing the properties of **2** in its HTS and LTS forms (Fig. 6). Comparing the emission from the HTS form of **2** to its LTS form, it can be noted that the emission remained centred at 520 nm, but revealed a slight broadening up to an FWHM of 59 nm (2119 cm^{-1}) and was accompanied by a reduced emission intensity (Fig. 6). In agreement with that observation, the lifetime dropped to 34.1 μs, while maintaining a monoexponential decay. This suggests increased structural flexibility of the HTS form which allows for increased phonon-mediated radiationless decay. It is also important to point out that multiple heating and cooling cycles across the solid–solid transition of **2** did not negatively affect the luminescent properties of the material. The two phases rather kept similar lifetimes and φ (measurable only for LTS) between the different cycles, further proving the reversibility of this transition (ESI, Fig. S25–S27†). This feature could make **2** feasible for application in optoelectronic devices as a luminescent thermometer. Foreseeing the application of **1–3** as an emitter in electrochemical devices, the electroluminescence of the neat compounds has been investigated with a high frequency (HF) Tesla generator at room temperature. Once exposed to the HF Tesla generator all the materials exhibited green light emission detectable with the naked eye when placed in vacuum-sealed Schlenk tubes (Fig. 7). Unfortunately, technical limitations prevented the collection of emission spectra.
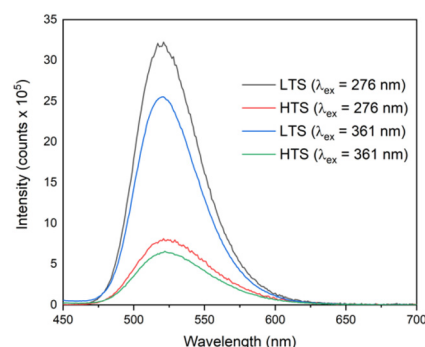

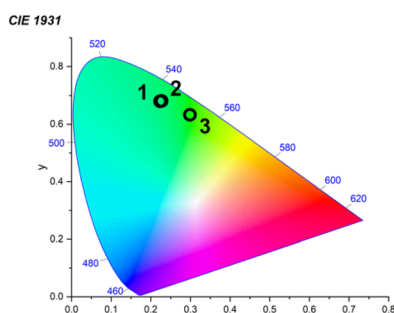**Fig. 6** Emission spectra of **2** in LTS (measured at RT) and HTS (measured at 80 °C.

Fig. 5 CIE1931 diagram for compounds **1–3** (the emission colour of **1** and **2** essentially overlap).

Fig. 7 Electroluminescence of materials **1–3**.

Electrochemical characterisation

To further explore the electrochemical behaviour, cyclic voltammetry was performed on solutions of **1–3**, see Fig. 8 and Table 4. The ferrocene/ferrocenium (Fc/Fc$^+$) redox couple was used as a reference, whose reversible redox process in acetonitrile has been determined to be 0.14 V. In this way, the HOMO energy level can be estimated according to the equation, $E_{HOMO} = -(E_{ox} + 4.8 - 0.14)$eV, with the absolute energy level of Fc/Fc$^+$ being 4.8 eV with respect to the vacuum level.[78] The obtained energies for **1** and **3** are essentially the same (−5.21 eV and −5.20 eV, respectively), while the one for **2** is marginally more negative (−5.31 eV). With the ΔE_λ values obtained from the UV-vis spectra of compounds **1–3**, it is also possible to estimate the LUMO energy levels as the difference between the HOMO energies and the ΔE_λ. This evaluation relies on the approximation that the lowest energy transition is essentially dominated by the excitation from the HOMO to the LUMO. Optical bandgaps (ΔE_λ) for **1–3** were determined as $1240/\lambda_{onset}$[nm], with λ_{onset} being the onset of the absorption bands at low energies (See ESI, Fig. S20†), corresponding to 2.63 eV (472 nm) for **1** and **2**, and 2.61 eV (475 nm) for **3** (Table 4). For comparison, a band gap of 2.62 eV has been reported for [N$_{4444}$]$_2$[MnBr$_4$].[39] Following the described procedure, the obtained LUMO energies are −2.58 eV (**1**), −2.68 eV (**2**), and −2.59 eV (**3**). Interestingly, these values match that of −2.77 eV predicted from spin-polarised DFT calculations for bis(piperidinium)tetrabromidomangante(II).[79] PDOS (projected density of states) analysis reveals the HOMO being of mostly Br–p character with Mn–d contributions and the LUMO predominately of Mn–d character. The organic countercations do not contribute to the frontier orbital region, which would also explain why the optical and electronic properties of the investigated complexes are, with respect to the energies, largely unaffected by the cation. Yet some shift of the half-wave potential can be seen in the CV for **2** compared to **1** and **3**. We have observed for other tetrabromido(II) complexes that

Table 4 Electrochemical properties of 1–3

Compound	ΔE_λ (eV)	E_{Ox}(v)	HOMO (eV)	LUMO (eV)
1	2.63	0.41	−5.21	−2.58
2	2.63	0.51	−5.31	−2.68
3	2.61	0.40	−5.20	−2.59

a structural change and, possibly, aggregation can occur under applied fields,[80] which could be an explanation for the observation.

Conclusions

Three new tetraalkylphosphonium tetrabromidomanganates(II) were synthesised from the respective tetraalkylphosphonium bromide and MnBr$_2$ in quantitative yield. Thermal analysis allows [P$_{4444}$]$_2$[MnBr$_4$] (**1**) and [P$_{8888}$]$_2$[MnBr$_4$] (**3**) to be classified as ionic liquids (ILs), with the former displaying a melting point of 68.4 °C and transition to an SmA mesophase at 22.0 °C. The latter retained an isotropic liquid state even at −60 °C. The thermal analysis combined with X-ray diffraction studies revealed that [P$_{4444}$]$_2$[MnBr$_4$] (**1**) and [P$_{6666}$]$_2$[MnBr$_4$] (**2**) adopt high-symmetry mesophases. Specifically, **1** exhibits a layered liquid crystalline phase, whilst **2** adopts a plastic crystalline state due to the size match of the high-symmetry cation and anion. The electronic states of the emissive Mn^{2+} centre were, to a first approximation, not affected by the counter cations and all materials showed a similar HOMO–LUMO gap of ∼2.6 eV. The photoemission is greatly affected by the ion dynamics, rendering compound **1**, which was based on phosphonium cations with the shortest alkyl chains, the material that exhibited the highest photoluminescence quantum yield of 61% and a lifetime of ∼150 μs. We find that the larger the cation and the softer the lattice, the lower the excited state lifetimes and quantum yields. Thus, the design concept of separating the Mn-centres by larger countercations to avoid self-quenching is counteracted by increased vibrational quenching brought about by larger cations. Consequently, an optimal balance between the two counteracting effects has to be found. A large Mn^{2+} separate cannot be solely regarded as a design concept for this class of compounds.

Compared to the reported [N$_{4444}$]$_2$[MnBr$_4$], all phosphonium compounds, but in particular [P$_{4444}$]$_2$[MnBr$_4$], show superior performance with respect to photoluminescent quantum yield and thermal stability. In addition, the compounds are not sensitive to the atmosphere, in particular humidity. As all compounds show electroluminescence detectable with the naked eye, they are interesting emitter materials for organic light-emitting devices.

Fig. 8 Cyclic voltammograms of **1–3** in acetonitrile solution.

Conflicts of interest

There are no conflicts to declare.

Acknowledgements

References

1 C. Furlani and A. Furlani, Absorption spectra of some tetra-halogenomanganates(II), *J. Inorg. Nucl. Chem.*, 1961, **19**, 51–60.

2 J. Bauri, R. B. Choudhary and G. Mandal, Recent advances in efficient emissive materials-based OLED applications: a review, *J. Mater. Sci.*, 2021, **56**, 18837–18866.

3 K. Schlingman, Y. Chen, R. S. Carmichael and T. B. Carmichael, , 25 Years of Light–Emitting Electrochemical Cells: A Flexible and Stretchable Perspective, *Adv. Mater.*, 2021, 2006863.

4 Y. Rodríguez-Lazcano, L. Nataf and F. Rodríguez, Electronic structure and luminescence of [(CH$_3$)4N]2MnX4 (X=Cl, Br) crystals at high pressures by time-resolved spectroscopy: Pressure effects on the Mn-Mn exchange coupling, *Phys. Rev. B: Condens. Matter*, 2009, **80**, 085115.

5 G. Hong, X. Gan, C. Leonhardt, Z. Zhang, J. Seibert, J. M. Busch and S. Bräse, A Brief History of OLEDs—Emitter Development and Industry Milestones, *Adv. Mater.*, 2021, **33**, 2005630.

6 H. Shin, Y. H. Ha, H. G. Kim, R. Kim, S. K. Kwon, Y. H. Kim and J. J. Kim, Controlling Horizontal Dipole Orientation and Emission Spectrum of Ir Complexes by Chemical Design of Ancillary Ligands for Efficient Deep–Blue Organic Light–Emitting Diodes, *Adv. Mater.*, 2019, **31**, 1808102.

7 Q. Li, C. Shi, M. Huang, X. Wei, H. Yan, C. Yang and A. Yuan, B- and N-embedded color-tunable phosphorescent iridium complexes and B–N Lewis adducts with intriguing structural and optical changes, *Chem. Sci.*, 2019, **10**, 3257–3263.

8 R. Bai, X. Meng, X. Wang and L. He, Blue–Emitting Iridium (III) Complexes for Light–Emitting Electrochemical Cells: Advances, Challenges, and Future Prospects, *Adv. Funct. Mater.*, 2020, **30**, 1907169.

9 C. Zhang, R. Liu, D. Zhang and L. Duan, Progress on Light–Emitting Electrochemical Cells toward Blue Emission, High Efficiency, and Long Lifetime, *Adv. Funct. Mater.*, 2020, **30**, 1907156.

10 J. E. Namanga, H. Pei, G. Bousrez, V. Smetana, N. Gerlitzki and A.-V. Mudring, Fluorinated Cationic Iridium(III) Complex Yielding an Exceptional, Efficient, and Long-Lived Red-Light-Emitting Electrochemical Cell, *ACS Appl. Energy Mater.*, 2020, **3**, 9271–9277.

11 J. E. Namanga, H. Pei, G. Bousrez, B. Mallick, V. Smetana, N. Gerlitzki and A. V. Mudring, Efficient and Long Lived Green Light–Emitting Electrochemical Cells, *Adv. Funct. Mater.*, 2020, **30**, 1909809.

12 M. S. Alsaeedi, Insight into luminescent iridium complexes: Their potential in Light-Emitting Electrochemical Cells, *J. Saudi Chem. Soc.*, 2022, 101442.

13 K. Li, Y. Chen, J. Wang and C. Yang, Diverse emission properties of transition metal complexes beyond exclusive single phosphorescence and their wide applications, *Coord. Chem. Rev.*, 2021, **433**, 213755.

14 H. Yersin, in *Transition Metal and Rare Earth Compounds: Excited States, Transitions, Interactions III*, ed. H. Yersin, Springer, Berlin, Heidelber, 2004.

15 J. H. Burroughes, D. D. Bradley, A. Brown, R. Marks, K. Mackay, R. H. Friend, P. L. Burns and A. B. Holmes, Light-emitting diodes based on conjugated polymers, *Nature*, 1990, **347**, 539–541.

16 A. R. Brown, K. Pichler, N. C. Greenham, D. D. C. Bradley, R. H. Friend and A. B. Holmes, Optical spectroscopy of triplet excitons and charged excitations in poly (p-phenylenevinylene) light-emitting diodes, *Chem. Phys. Lett.*, 1993, **210**, 61–66.

17 M. A. Baldo, M. E. Thompson and S. R. Forrest, Phosphorescent materials for application to organic light emitting devices, *Pure Appl. Chem.*, 1999, **71**, 2095–2106.

18 M. A. Baldo, D. F. O'brien, M. E. Thompson and S. R. Forrest, Excitonic singlet-triplet ratio in a semiconducting organic thin film, *Phys. Rev. B: Condens. Matter*, 1999, **60**, 14422.

19 T. Fleetham, G. Li and J. Li, Phosphorescent Pt(II) and Pd (II) complexes for efficient, high–color–quality, and stable OLEDs, *Adv. Mater.*, 2017, **29**, 1601861.

20 K. E. Lawson, Optical Studies of Electronic transitions in hexa–and tetracoordinated Mn2+crystals, *J. Chem. Phys.*, 1967, **47**, 3627–3633.

21 M. T. Vala, C. J. Ballhausen, R. Dingle and S. L. Holt, Tetrahedral transition-metal complex spectra, *Mol. Phys.*, 1972, **23**, 217–234.

22 F. A. Cotton, D. M. Goodgame and M. Goodgame, Absorption spectra and electronic structures of some tetrahedral manganese(II) complexes, *J. Am. Chem. Soc.*, 1962, **84**, 167–172.

23 P. Tao, S. J. Liu and W. Y. Wong, Phosphorescent Manganese(II) Complexes and Their Emerging Applications, *Adv. Opt. Mater.*, 2020, **8**, 2000985.

24 S. Pitula and A.-V. Mudring, Synthesis, Structure, and Physico-optical Properties of Manganate(II)-Based Ionic Liquids, *Chem. – Eur. J.*, 2010, **16**, 3355–3365.

25 Y. Zhang, W.-Q. Liao, D.-W. Fu, H.-Y. Ye, Z.-N. Chen and R.-G. Xiong, Highly Efficient Red-Light Emission in An Organic–Inorganic Hybrid Ferroelectric: (Pyrrolidinium) MnCl3, *J. Am. Chem. Soc.*, 2015, **137**, 4928–4931.

26 Y. Zhang, W.-Q. Liao, D.-W. Fu, H.-Y. Ye, C.-M. Liu, Z.-N. Chen and R.-G. Xiong, The First Organic–Inorganic

Hybrid Luminescent Multiferroic: (Pyrrolidinium)MnBr3, *Adv. Mater.*, 2015, **27**, 3942–3946.

27 V. Morad, I. Cherniukh, L. Pöttschacher, Y. Shynkarenko, S. Yakunin and M. V. Kovalenko, Manganese(II) in Tetrahedral Halide Environment: Factors Governing Bright Green Luminescence, *Chem. Mater.*, 2019, **31**, 10161–10169.

28 L. Mao, P. Guo, S. Wang, A. K. Cheetham and R. Seshadri, Design Principles for Enhancing Photoluminescence Quantum Yield in Hybrid Manganese Bromides, *J. Am. Chem. Soc.*, 2020, **142**, 13582–13589.

29 L.-J. Xu, C.-Z. Sun, H. Xiao, Y. Wu and Z.-N. Chen, Green-Light-Emitting Diodes based on Tetrabromide Manganese (II) Complex through Solution Process, *Adv. Mater.*, 2017, **29**, 1605739.

30 M. Worku, Y. Tian, C. Zhou, S. Lee, Q. Meisner, Y. Zhou and B. Ma, Sunlike White-Light-Emitting Diodes Based on Zero-Dimensional Organic Metal Halide Hybrids, *ACS Appl. Mater. Interfaces*, 2018, **10**, 30051–30057.

31 Y. Qin, P. She, X. Huang, W. Huang and Q. Zhao, Luminescent manganese(II) complexes: Synthesis, properties and optoelectronic applications, *Coord. Chem. Rev.*, 2020, **416**, 213331.

32 J.-C. Chang, W.-Y. Ho, I.-W. Sun, Y.-K. Chou, H.-H. Hsieh and T.-Y. Wu, Synthesis and properties of new tetrachloro-cobaltate(II) and tetrachloromanganate(II) anion salts with dicationic counterions, *Polyhedron*, 2011, **30**, 497–507.

33 S. Pohl, W. Saak and P. Stolz, (Ph4P) 2 Mn2Br6 und (Ph3PCH2Ph) 2Mn2I6 (Ph = C6H5)/(Ph4P) 2Mn2Br6 and (Ph 3PCH2Ph) 2Mn2I6 (Ph = C6H5, *Z. Naturforsch. B.*, 1988, **43**, 171–174.

34 P. She, Y. Ma, Y. Qin, M. Xie, F. Li, S. Liu, W. Huang and Q. Zhao, Dynamic luminescence manipulation for rewritable and multi-level security printing, *Matter*, 2019, **1**, 1644–1655.

35 Y. Qin, P. She, S. Guo, X. Huang, S. Liu, Q. Zhao and W. Huang, Structural manipulation and triboluminescence of tetrahalomanganese(II) complexes, *Acta. Phys.-Chim. Sin.*, 2020, **36**, 1907078.

36 F. A. Cotton, L. M. Daniels and P. Huang, Correlation of structure and triboluminescence for tetrahedral manganese(II) compounds, *Inorg. Chem.*, 2001, **40**, 3576–3578.

37 H.-Q. Ye, Y.-L. Qian, Y.-H. Pan, M.-N. Li, X.-n. Lin, X.-X. Zheng, H.-T. Cai, X.-P. Liu, L.-M. Yang and J.-R. Zhou, Syntheses, Crystal Structures, and Weak Interactions of Two 4-Substituted Benzyl Triphenylphosphonium Salts Containing Tetrachloromanganate(II) Anion, *Synth. React. Inorg., Met.-Org., Nano-Met. Chem.*, 2016, **46**, 495–501.

38 W.-Q. Chen, D.-D. Zhou, M.-H. Feng, Y.-Q. Peng, S. Han, X. Chen, X.-P. Liu, L.-M. Yang, J.-R. Zhou and C.-L. Ni, Syntheses, crystal structures, weak interactions, and magnetic properties of two tetrachloromanganate(II) salts with substituted benzyl triphenylphosphonium, *Synth. React. Inorg., Met.-Org., Nano-Met. Chem.*, 2012, **42**, 857–863.

39 A. Jana, S. Zhumagali, Q. Ba, A. S. Nissimagoudar and K. S. Kim, Direct emission from quartet excited states triggered by upconversion phenomena in solid-phase syn-thesized fluorescent lead-free organic–inorganic hybrid compounds, *J. Mater. Chem. A*, 2019, **7**, 26504–26512.

40 E. Jalilian and S. Lidin, Bis (isopropyl-triphenylphosphonium) di-μ-iodido-bis [iodidocopper(I)], *Acta Crystallogr., Sect. E: Struct. Rep. Online*, 2010, **66**, m432–m433.

41 A. Ben Akacha, C. Zhou, M. Chaaban, D. Beery, S. Lee, M. Worku, X. Lin, R. Westphal and B. Ma, Mechanochemical Synthesis of Zero Dimensional Organic–Inorganic Metal Halide Hybrids, *ChemPhotoChem*, 2021, **5**, 326–329.

42 B. Howard and B. R. Sundheim, Fluorescence of Mn(II) in Molten Salts, *J. Chem. Phys.*, 1969, **50**, 5035–5035.

43 H. Mashiyama and N. Koshiji, A structural study of phase transitions in [N (CH₃) 4] 2MnCl4, *Acta Crystallogr., Sect. B: Struct. Sci.*, 1989, **45**, 467–473.

44 N. Koshiji and H. Mashiyama, Disordered and displacive models for the structure of the normal phase in {N (CH 3) 4} 2 MnCl 4, *J. Phys. Soc. Jpn.*, 2000, **69**, 3853–3859.

45 P. Moews Jr., The crystal structure, visible, and ultraviolet spectra of potassium hexachloromanganate(IV), *Inorg. Chem.*, 1966, **5**, 5–8.

46 K. Hasebe and T. Asahi, Structure of tetramethyl-ammonium tetrabromomanganate at room temperature, *Acta Crystallogr., Sect. C: Struct. Chem.*, 1989, **45**, 841–843.

47 K. Hasebe, T. Asahi and K. Gesi, Structure of tetramethyl-ammonium tetrabromomanganate in its low-temperature phase, *Acta crystallogr., C Struct. chem.*, 1990, **46**, 759–762.

48 S. Chen, J. Gao, J. Chang, Y. Zhang and L. Feng, Organic-inorganic manganese(II) halide hybrids based paper sensor for the fluorometric determination of pesticide ferbam, *Sens. Actuators B: Chem.*, 2019, **297**, 126701.

49 I. Dhouib, A. Ouasri and Z. Elaoud, Disordered structures, vibrational spectroscopy, thermal behavior, and electrical properties of two new tetrachlorometallates complexes [(CH3CH2CH2)4N]2MIICl4 with MII = Co and Mn, *J. Saudi Chem. Soc.*, 2020, **24**, 567–583.

50 E. Styczeń, Z. Warnke, D. Wyrzykowski, J. Kłak, J. Mroziński and A. Sikorski, Bis(tetraethylammonium) tetrabromocobaltate(II) and bis(tetrabutylammonium) tetrabromomanganate(II): structure and magnetic properties, *Struct. Chem.*, 2010, **21**, 269–276.

51 Y.-Y. Luo, Z.-X. Zhang, C.-Y. Su, W.-Y. Zhang, P.-P. Shi, Q. Ye and D.-W. Fu, Tunable optoelectronic response multifunctional materials: exploring switching and photoluminescence integrated in flexible thin films/crystals, *J. Mater. Chem. C*, 2020, **8**, 7089–7095.

52 Y. Wu, W. Fan, Z. Gao, Z. Tang, L. Lei, X. Sun, Y. Li, H.-L. Cai and X. Wu, New photoluminescence hybrid perovskites with ultrahigh photoluminescence quantum yield and ultrahigh thermostability temperature up to 600 K, *Nano Energy*, 2020, **77**, 105170.

53 R. E. Del Sesto, C. Corley, A. Robertson and J. S. Wilkes, Tetraalkylphosphonium-based ionic liquids, *J. Organomet. Chem.*, 2005, **690**, 2536–2542.

54 M. Wolff, K. Alexander and G. Belder, Uses of quaternary phosphonium compounds in phase transfer catalysis, *Chim. Oggi*, 2000, **18**, 29–32.

55 K. J. Fraser and D. R. MacFarlane, Phosphonium-Based Ionic Liquids: An Overview, *Aust. J. Chem.*, 2009, **62**, 309–321.

56 R. Dobužinskas, A. Poškus, M. Viliūnas, V. Jankauskas, M. Daškevičienė, V. Getautis and K. Arlauskas, Melt Spin Coating for X-Ray-Sensitive Hybrid Organic–Inorganic Layers of Small Carbazolyl-Containing Molecules Blended with Tungsten, *Phys. Status Solidi A*, 2019, **216**, 1900635.

57 C. J. Bradaric, A. Downard, C. Kennedy, A. J. Robertson and Y. Zhou, Industrial preparation of phosphonium ionic liquids, *Green Chem.*, 2003, **5**, 143–152.

58 G. Sheldrick, SHELXT - Integrated space-group and crystal-structure determination, *Acta Crystallogr. Sect. A: Found. Crystallogr.*, 2015, **71**, 3–8.

59 O. V. Dolomanov, L. J. Bourhis, R. J. Gildea, J. A. K. Howard and H. Puschmann, OLEX2: a complete structure solution, refinement and analysis program, *J. Appl. Crystallogr.*, 2009, **42**, 339–341.

60 G. Sheldrick, Crystal structure refinement with SHELXL, *Acta crystallogr., C Struct. chem.*, 2015, **71**, 3–8.

61 K. Brandenburg and H. Putz, Diamond: Program for Crystal and Molecular Structure Visualization, *Crystal Impact*, 2011.

62 C. F. Macrae, I. Sovago, S. J. Cottrell, P. T. A. Galek, P. McCabe, E. Pidcock, M. Platings, G. P. Shields, J. S. Stevens, M. Towler and P. A. Wood, Mercury 4.0: from visualization to analysis, design and prediction, *J. Appl. Crystallogr.*, 2020, **53**, 226–235.

63 J. Weidlein, U. Müller and K. Dehnicke, *Schwingungsfrequenzen II*, Thieme, Stuttgart, 1986.

64 T. Steiner, The Hydrogen Bond in the Solid State, *Angew. Chem., Int. Ed.*, 2002, **41**, 48–76.

65 J. M. Pringle, P. C. Howlett, D. R. MacFarlane and M. Forsyth, Organic ionic plastic crystals: recent advances, *J. Mater. Chem.*, 2010, **20**, 2056–2062.

66 D. R. MacFarlane and M. Forsyth, Plastic Crystal Electrolyte Materials: New Perspectives on Solid State Ionics, *Adv. Mater.*, 2001, **13**, 957–966.

67 D. R. MacFarlane, P. Meakin, N. Amini and M. Forsyth, Structural studies of ambient temperature plastic crystal ion conductors, *J. Phys.: Condens. Matter*, 2001, **13**, 8257–8267.

68 B. Mallick, A. Metlen, M. Nieuwenhuyzen, R. D. Rogers and A.-V. Mudring, Mercuric Ionic Liquids: [Cnmim][HgX3], Where n = 3, 4 and X = Cl, Br, *Inorg. Chem.*, 2012, **51**, 193–200.

69 G. Bousrez, O. Renier, S. P. Kelley, B. Adranno, E. Tahavori, H. M. Titi, V. Smetana, S.-F. Tang, A. V. Mudring and R. D. Rogers, Ready access to anhydrous anionic lanthanide acetates using imidazolium acetate ionic liquids as the reaction medium, *Chem. – Eur. J.*, 2021, 202100141.

70 P. Wasserscheid and T. Welton, *Ionic liquids in synthesis*, Wiley Online Library, 2008.

71 A.-V. Mudring, Solidification of Ionic Liquids: Theory and Techniques, *Aust. J. Chem.*, 2010, **63**, 544–564.

72 J. O. Valderrama and L. F. Cardona, Predicting the melting temperature and the heat of melting of ionic liquids, *J. Ion. Liq.*, 2021, **1**, 100002.

73 J. Timmermans, A new mesomorphic state. Plastic organic crystals, *J. Chim. Phys.*, 1938, **35**, 331–344.

74 L. Wang, J. Zhao, N. Zhao, R. Zhou and B. Qu, Quantitative insights into the chemical trend of four-coordinated Mn^{2+} emission in inorganic compounds, *J. Lumin.*, 2020, **225**, 117399.

75 H. S. Fairman, M. H. Brill and H. Hemmendinger, How the CIE 1931 color-matching functions were derived from Wright-Guild data, *Color Res. Appl.*, 1997, **22**, 11–23.

76 M. Wrighton and D. Ginley, Excited State Decay Of Tetrahalomancanesejii Complexes, *Chem. Phys.*, 1974, **5**, 295–299.

77 J. Chen, Q. Zhang, F.-K. Zheng, Z.-F. Liu, S.-H. Wang, A. Q. Wu and G.-C. Guo, Intense photo- and tribo-luminescence of three tetrahedral manganese(II) dihalides with chelating bidentate phosphine oxide ligand, *Dalton Trans.*, 2015, **44**, 3289–3294.

78 Y. Fang, J. Liu, Y. Zhang, T. Guo, F. Huang, W. Yang and Y. Cao, Blue light-emitting polyfluorenes containing dibenzothiophene-S,S-dioxide unit in alkyl side chain, *Sci. China: Chem.*, 2017, **60**, 1356–1366.

79 T. Huang, Q. Wei, W. Lin, H. Peng, S. Yao and B. Zou, High-efficient yellow-green emission in $(TDMP)MnBr_4$ single crystal with modulation of spin-phonon-charge interactions, *Mater. Today Phys.*, 2022, **25**, 100703.

80 B. Adranno, S. Tang, V. Paterlini, V. Smetana, O. Renier, G. Bousrez, L. Edman and A.-V. Mudring, Broadband white light-emitting light emitting electrochemical cells, *Adv. Photonics Res.*, 2023, 2200351.